Applied Surface Science 588 (2022) 152927

Contents lists available at ScienceDirect

Applied Surface Science

journal homepage: www.elsevier.com/locate/apsusc

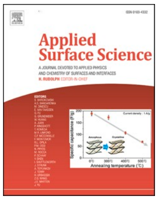

Full Length Article

Which factor determines the optical losses in refractory tungsten thin films at high temperatures?

Mahima Arya [a,1], Ankita Ganguly [a,1], Gnanavel V. Krishnamurthy [b,1], Surya S. Rout [c], Leonid Gurevich [d], Tobias Krekeler [c], Martin Ritter [c], Kjeld Pedersen [d], Michael Störmer [b], Alexander Yu Petrov [a,b,e], Manfred Eich [a,b], Manohar Chirumamilla [a,d,*]

[a] Institute of Optical and Electronic Materials, Hamburg University of Technology, Hamburg 21073, Germany
[b] Institute of Materials Research, Helmholtz-Zentrum Geesthacht Centre for Materials and Coastal Research, Geesthacht 21502, Germany
[c] Electron Microscopy Unit, Hamburg University of Technology, Hamburg 21073, Germany
[d] Department of Materials and Production, Aalborg University, Skjernvej 4A, Aalborg Øst 9220, Denmark
[e] ITMO University, 49 Kronverskii Avenue, Saint Petersburg 197101, Russia

ARTICLE INFO

Keywords:
Tungsten
Thin films
High temperature stability
Electron–phonon interaction
Grain boundary scattering
Surface scattering
Thermophotovoltaics

ABSTRACT

Refractory tungsten (W) plays an important role in high temperature photonic/plasmonic applications. Previously room temperature bulk single/poly-crystalline optical constants were extensively used to calculate the optical properties of W nanostructures at high temperatures. This might lead to a significant deviation between the predicted and measured optical properties due to the exclusion of electron–phonon interaction, as well as grain-boundary and surface-scattering.

Herein, we show experimentally, how film thickness and temperature affects the optical losses in W. A drastic increase in the effective electron collision frequency is observed with decreasing the film thickness down to 5 nm, due to the grain-boundary and surface-scattering mechanisms. At sufficiently high temperatures (greater than 200 °C for W), the electron–phonon interaction eventually becomes the dominant mechanism, linearly increasing collision frequency with temperature, and it is independent of the geometry of the thin film structure. The impact of thickness and temperature-dependent optical properties of W is showcased with a hyperbolic 1D metamaterial structure acting as a thermophotovoltaic emitter. This work opens new directions in accurate prediction of the optical properties of nanostructures and design of efficient devices in various applications, such as aerospace, energy-efficient lighting, radiative cooling and energy harvesting, by incorporating thickness and temperature-dependent optical constants.

1. Introduction

W, a refractory material, plays a vital role in broadband absorption [1–2], aerospace [3–4], energy-efficient lighting [5], thermoplasmonics [6–7] and especially in thermophotovoltaic (TPV) [2,8–9] applications. The optical properties of W exhibit a positive real part of the complex dielectric permittivity, an imaginary part with a magnitude on par with the real part below a wavelength of 900 nm, and a negative real part of the complex dielectric permittivity in the near-far infrared spectral regions. Therefore, W based nanostructures are widely used as broadband absorbers in the visible and near-infrared regions, and as spectrally selective emitters in TPV to minimize the thermal emission in the near-mid infrared range [1–2,10]. In TPV, the emitter will be heated to 1000 °C or higher. According to the Stefan-Boltzmann law [11–12], the radiative power of the blackbody is proportional to T^4. Therefore, high operating temperatures enhance the efficiency of TPV systems. Also, the peak emission shifts to shorter wavelengths proportional to the black body temperature, thus allowing higher conversion efficiencies through the use of larger bandgap semiconductors, such as Si, GaSb, etc. They are better developed (for large open-circuit voltage and low short-circuit current) and provide higher conversion efficiencies as their lower bandgap counterparts [13]. Bierman et al. [14] showed that when a back-side reflector is used underneath the PV cell, the thermalization losses were reduced in the system with the increased bandgap energy.

---

* Corresponding author.
E-mail addresses: mch@mp.aau.dk, manohar.chirumamilla@tuhh.de (M. Chirumamilla).

[1] Equal authorship

https://doi.org/10.1016/j.apsusc.2022.152927
Received 22 September 2021; Received in revised form 23 February 2022; Accepted 24 February 2022

Thus, understanding the optical properties of W at high temperatures is crucial for these and any other applications, where thin film geometries are needed to construct plasmonic/photonic structures. However, due to the lack of appropriate W optical constants at elevated temperatures, room temperature (RT) bulk substrate (either poly crystalline or single crystalline, PC or SC, respectively) data from a limited spectral range are often used to calculate the spectral response of nanostructures at high temperatures [15–22].

Moreover, current research in the field involves W nanostructured metallic films of various thicknesses in the range of 10 nm to 100 nm, to tailor the light absorption/emission. For this, bulk substrate optical constants were used to calculate the optical properties of these nanostructures [1–2,8,23]. It is important to note that the optical properties of thin metallic films are highly affected by the growth conditions [24–25], grain size [26–27], crystallinity [28–29], defects [24,30] and thickness of the film [31–33]. Optical constants of bulk metals should therefore not be used to model nanometric thin films, as the thickness of the film changes the magnitude of the optical constants substantially.

There are several studies on the thickness and temperature-dependent optical properties of various noble metals, such as Au [27,33–34], Ag [29,31,32], etc. However, when the film thickness is in the order of 10 nm or less, non-uniform or even semi-continuous layers are formed [32–33,35]. For refractory metals, such as W [18,25,36–38], Mo [18,25,36,39], TiN [40–42], etc., studies of the combination of thickness and temperature-dependent optical properties are largely absent. In thin films, when the grain size and/or thickness is in the order of the electron–phonon collision mean free path at a particular temperature [26,43–45], electron scattering at grain boundaries and film surfaces contributes strongly to the optical losses in the metal. Increase in the collision frequency has an intricate influence on the complex permittivity of metal, and it can be estimated with the Drude model [46]. Near the plasma frequency, it generally leads to an increasing imaginary ε_2 part and a reduction of the amplitude of the real $|\varepsilon_1|$ part of the complex dielectric permittivity. At high temperatures, thermal phonon interaction with the electrons will amplify the optical losses in the thin film structures. Thus, by neglecting the thickness and temperature-dependent optical losses in simulations, the calculated optical properties of the nanostructures are inaccurate [2,8,20–22]. Therefore, to design efficient structures, it is imperative to investigate the optical properties of W thin films at high temperatures. So far, the temperature-dependent optical properties of W have been studied in the visible-mid infrared spectral region only for a bulk PC substrate at temperatures up to 400 °C under ambient atmosphere [18]. T. Smith [47] reported the optical properties of the W at two distinct wavelengths of 546 nm and 632 nm, after annealing at temperatures higher than 1300 °C. The visible only wavelengths used here cannot unveil the qualitatively different material response observed at infrared wavelengths as mainly used in our study. Further, P. Wells et al. [36] demonstrated a significant change in the magnitude of the W optical constants (between 50% and 100%) after heating an 80 nm d_w structure to 300 °C – 500 °C for 1 h under ambient atmosphere. A complete degradation of the W spectral features was noticed after heating at 400 °C. The formation of W-oxides was clearly seen in the X-ray analysis of the W structure after heating at 500 °C under an ambient atmosphere.

J. I. Watjen et al. [37] reported room temperature optical properties of a 70 nm thick poly crystalline film structure before and after annealing at 800 °C for 1 h. The importance of α-phase W in thin films was explored to achieve bulk-like optical properties. W is thermally stable when it is in the α-phase (bcc-A2 structure and lattice parameter a = 0.3165 nm) [48–50]. M. Minissale et al. [38] reported in-situ temperature-dependent optical properties of a W bulk substrate in a limited spectral region between 500 nm and 1050 nm and at operating temperatures up to 650 °C under a low vacuum pressure of 10^{-3} mbar. After heating the W substrate at high temperatures (a cumulative time of 12 h and 3 h between 245 °C and 275 °C, and 425 °C-650 °C, respectively), oxidization of W was observed. Therefore, to prevent oxidization [51–52], it is essential to use high vacuum conditions at elevated temperatures while evaluating the optical properties of W. To the best of our knowledge, no experimental work has been presented investigating the in-situ optical properties of W (neither bulk substrate nor thin film structures) at temperatures up to 1000 °C in the visible-mid infrared spectral regions under O_2 free atmosphere.

In this work a comprehensive study is performed to address the challenges of investigating the optical properties of W thin films at high temperatures under O_2 free atmosphere, W thin films with various thicknesses (between 5 nm and 160 nm), along with SC and PC W substrates, are investigated at temperatures from RT to 1000 °C. An in-situ ellipsometer operating in the visible-mid infrared range and equipped with a heating chamber under a high vacuum condition is used to characterize the W structures at elevated temperatures. A significant change in the optical constants of the W is observed with temperature and thickness, due to electron–phonon interaction and, grain boundary and surface scattering mechanisms, respectively.

The accuracy of the measured optical constants for thin films was verified with a hyperbolic multilayer metamaterial emitter. At RT, ~95% of the spectral match is observed between the calculated and measured absorptivity/emissivity spectra when the optical constants of measured W thin films are used. However, a substantial difference (2–5 × in the absorptivity/emissivity at the near-infrared region) is noticed when the bulk optical constants of W are used. Further, the emissivity of the metamaterial emitter at elevated temperatures was calculated using the measured in-situ optical constants at high temperatures. When the temperature raises, the calculated absorptivity/emissivity of the emitter in the long-wavelength range will increase significantly. Thus, the emitter will show a loss in spectral selectivity at high temperatures. These results advance the understanding of the optical properties of W-based structures at high temperatures and demonstrate a crucial step towards designing efficient devices for thermo photonic/plasmonic applications. Although herein we report exclusively the temperature and thickness-dependent optical properties of W, these loss mechanisms can be quantitatively applied as a starting point to evaluate other metals.

2. Experimental Section/Methods

2.1. *W Structure fabrication*

W thin film structures with various thicknesses d_W: 5, 10, 20, 40, 80 and 160 nm, are deposited onto cleaned 10 × 10 mm^2 single-crystalline sapphire substrates ([1–102] orientation) by direct current (DC) magnetron sputtering, at RT with a rate of 0.09 nms^{-1}, and at argon (99.99999%) gas pressure of 2×10^{-3} mbar. The base pressure of the sputtering chamber was kept below 10^{-7} mbar. The W sputtering target with 99.95% purity was purchased from Sindlhauser Materials. PC W substrates were purchased from MTI corporation, and SC W substrates were purchased from MaTecK GMBH.

2.2. *XRD measurements*

XRD measurements were conducted using a Bruker D8 advanced diffractometer. Cu Kα (λ = 0.15405 nm) radiation was used to investigate thin film structures. The measurements were performed using parallel beam geometry. The diffraction patterns (2θ from 20° to 90°) were recorded with an increment of 0.04° and a step time of 16 s. The film thicknesses were measured precisely by X-ray reflectometry (XRR) analyses, and evaluated by fitting simulations to experimental reflectivity scans with the Leptos R software package (Bruker AXS).

2.3. *In-situ ellipsometry*

The in-situ temperature dependent optical constants of the W structures with various film thicknesses and SC/PC W substrates, are measured by a spectroscopic ellipsometer (Semilab SE-2000), at an incident angle of 70°, in the visible-mid infrared region (500 nm-15000 nm). The W sample was mounted onto a heating stage (Linkam Scientific Model TSEL1000V). The heating stage equipped with a ceramic heating cup, which is controlled through the Linkam T96-S temperature controller. The heating stage contains two side quartz/ZnSe windows (for visible to near-infrared/near-infrared to mid-infrared ranges, respectively), fixed at an angle of 70°, along the polarizer and analyzer arms of the ellipsometer, and a centre quartz window for the sample inspection. The heating stage is connected to a TPS-flexy turbo pumping system (X1699-64078, from Agilent technologies), and a high vacuum pressure of 2×10^{-5} mbar is maintained during high temperature operation. A CCD spectrograph and InGaAs linear array detectors are used in the spectroscopic ellipsometer in the wavelength ranges of 500 nm-900 nm and 900 nm-2100 nm, respectively, whereas a Mercury-Cadmium-Telluride (MCT) detector is used for 2100 nm-15000 nm spectral range. The W samples were heated between 20 °C and 1000 °C with a step size of 100 °C and a ramp rate of 30 °C/min. Where, at each measuring temperature, the sample was kept for 10 min to achieve thermalization with the heating element, and then measurements were taken. For the sake of presentation clarity, the data points were shown for every 200 °C step size. An external water-cooling unit is connected to the heating stage to cool the side windows at high operating temperatures. The real and imaginary parts of the W complex dielectric functions were extracted from the measured Ψ and Δ using Semilab's SEA software and a model containing a Drude and four Lorentz oscillators. The quality of the fit is explained in the form of R^2, it is the coefficient of determination and measures the agreement between measured data and the fitted model with a particular choice of parameters. R^2 values range from 0 to 1, where 1 represents a good agreement between the measured and fitted data, and 0 indicates that the model has no ability to interpret the variance in the measured data. The R^2 parameter is given by

$$R^2 = 1 - \frac{1}{2}\frac{A}{C} - \frac{1}{2}\frac{B}{D}$$

with

$$A = \sum_{i=1}^{N} \left(\frac{f^i_{1,meas} - f^i_{1,calc}}{\sigma^i_{1,meas}}\right)^2$$

$$B = \sum_{i=1}^{N} \left(\frac{f^i_{2,meas} - f^i_{2,calc}}{\sigma^i_{2,meas}}\right)^2$$

$$C = \sum_{i=1}^{N} \left(\frac{f^i_{1,meas} - \overline{f_{1,meas}}}{\sigma^i_{1,meas}}\right)^2$$

$$D = \sum_{i=1}^{N} \left(\frac{f^i_{2,meas} - \overline{f_{2,meas}}}{\sigma^i_{2,meas}}\right)^2$$

Here, N is the number of measuring points, f^i_{meas}andf^i_{calc} are the i^th measured and calculated ellipsometric quantities, σ^i_1andσ^i_2 are the pointwise experimental errors corresponding to the f_1 and f_2 measurements.

2.4. Thermal stability of W structure

The long-term thermal stability of the W structure is investigated using a high-temperature vacuum furnace (RD-G WEBB) at 1000 °C and durations up to 120 h under 2×10^{-6} mbar pressure. The temperature was ramped at a rate of 10 $^\circ\mathrm{Cmin}^{-1}$. Vacuum conditions, low (rough) vacuum: Atm. pressure to 1 mbar, medium vacuum: 1 to 10^{-3} mbar, high vacuum: 10^{-3} to 10^{-8} mbar, ultrahigh vacuum: 10^{-8} to 10^{-12} mbar and extreme high vacuum: less than10^{-12} mbars [53].

2.5. Reflectivity measurements

Reflectivity spectra of the W thin film structures and 1D hyperbolic metamaterial structures were measured using UV–Vis-NIR and Fourier transform infrared (FTIR) spectrometers. A PerkinElmer Lambda 1050 spectrometer with a wavelength scan step of 5 nm is used to measure the reflectivity in the wavelength range of 0.5 to 2.0 μm. A labsphere spectralon reflectance standard is used for normalization. The incident light is unpolarized, and the minimum angle of incidence of the system is 8°. An FTIR microscope (Bruker Hyperion 2000) with a 15 × Schwarzschild objective coupled to an FTIR spectrometer (Bruker Vertex 70) is used to measure the reflectivity in the range 2 to 4 μm, where an Au mirror is used for normalization. The objective operates ~16° off-normal to the sample surface and has a collection cone apex angle of ± 7°. The optical absorptivity α is obtained by $\alpha = 1 - \rho - \tau$, where ρ and τ are reflectivity and transmissivity. Due to a 100 nm thick bottom W layer, $\tau = 0$ in the measured spectral range. Thus, absorptivity, $\alpha = 1 - \rho$, can be directly deduced from the reflection spectra.

2.6. Morphology and elemental analysis of the W structures

Cross-sectional TEM samples of the W structures were prepared with a focused-ion beam scanning electron microscope (FIB-SEM, FEI Helios G3 UC) machine using a 30 keV Ga ion beam and transferred to Cu lift-out grids via in-situ lift-out technique. To prevent charging during FIB preparation, the samples were coated with a 10 nm-20 nm layer of C, by a C thread evaporator. The final thickness of the lamellae was less than 100 nm. An FEI Talos F200X TEM equipped with a high brightness Schottky-FEG (X-FEG) and a four-quadrant SDD-EDS system (solid angle of 0.9 srad) was used for EDS analysis. 512 × 512 pixel spectrum images were obtained using a probe current of 1nA and a dwell time of 10 μs per pixel. Thermo Fischer Scientific Velox software was used for data acquisition and visualization. For the spectrum images, the energies of the following elements were used: Al-K_α (1.49 keV), O-K_α (0.52 keV) and W-M_α (1.77 keV).

2.7. AFM topography

The topography images were acquired with an NTegra Aura AFM (NT-MDT, Russia) operating in a tapping mode. HA_HR cantilevers (ScanSens, Germany) with a nominal force constant 34 N/m, a resonance frequency of 380 kHz, and a tip radius of 10 nm were used for imaging. The images were processed with free WSxM software [54]. The root-mean-square (RMS) surface roughness values were evaluated.

Grain size analysis was performed with a MountainSPIP 8 (Digital Surf, France) software using Hills and Valleys particle analysis procedure. Briefly, grains in an AFM image were identified using the watershed algorithm. Then, each grain was labelled, and the projected area of each grain was calculated. The average projected area yielded an averaged grain size in the film. The watershed algorithm is quite robust against tip convolution effects, assuming that there are no double/multiple tip artefacts, and the tip curvature is smaller than the grain size, which could be easily achieved in this case since fresh tips were used. The images for processing were visually inspected for the absence of artefacts (double tip, drift etc.) before processing.

3. Results and discussion

The schematic of the W structure deposited on a SC-Al_2O_3 (1–102) substrate by direct current (DC) magnetron sputter deposition is shown in Fig. 1a. W structures with various thicknesses d_W (d_W = 5, 10, 20, 40, 80 and 160 nm) are fabricated. As an example, a high-resolution transmission electron microscopy (HRTEM) image of the 5 nm d_W structure shown in Fig. 1b clearly highlights the nanostructure homogeneity with a continuous W layer. Further, the uniformity of the 5 nm thin W structure over a large area (of 2.25 μm) is shown in Fig. S1. The

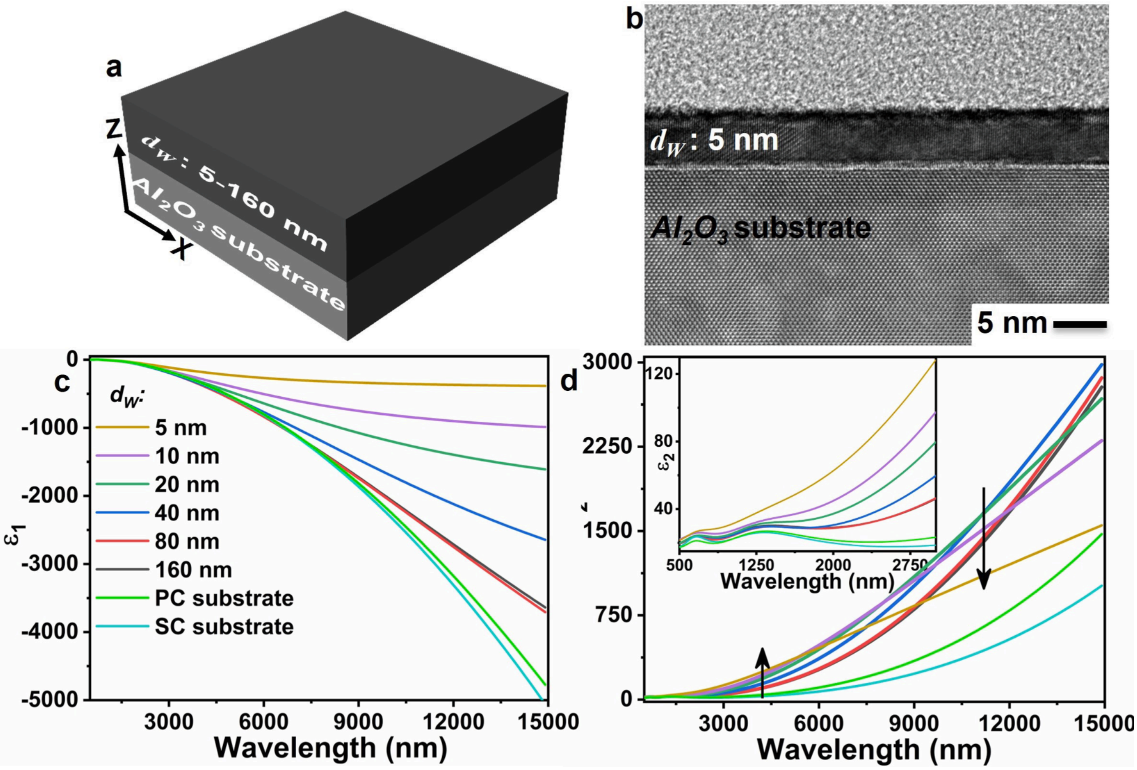

Fig. 1. a) Schematic of the W structure, where d_W represents the thickness of the W film. b) HRTEM image of a 5 nm d_W film deposited on single crystalline Al_2O_3 substrate ([1–102] orientation). Note that a protective carbon top layer is deposited before FIB milling to protect the W film during specimen preparation. c, d) The real and complex dielectric permittivities, ε_1 and ε_2, respectively, of the W structure with different thicknesses, d_W varying from 5 nm to 160 nm are extracted from spectroscopic ellipsometer measurements. The change in ε_2 at visible to near-infrared and mid-infrared regions are explained using Eq. (3) and (4).

energy-dispersive X-ray spectroscopy (EDS) analyses (Fig. S2) show that the as-fabricated W structure is free from O_2 contamination and other defects such as voids or pinholes (Fig. 1b).

Fig. 1c, d show the complex dielectric permittivities, real (ε_1) and imaginary (ε_2) parts, respectively, of the W structures taken at RT with various d_W ranging from 5 nm to 160 nm, in the spectral range of 500 nm to 15000 nm. The complex dielectric permittivities are evaluated by fitting a Drude-Lorentz oscillator model (Eq. (1)) based on the Rakic model [17], where the conduction electron contribution and interband transitions are expressed by Drude and Lorentz terms, respectively. The optical properties of the metal due to the freeelectron contribution in the infrared range are mainly determined by the Drude term. In the UV–visible range, the Lorentz term describes the interband transitions at the *d*-electronic bands.

$$\varepsilon(\omega) = \varepsilon_1 + i\varepsilon_2 = \varepsilon_\infty - \frac{\omega_p^2}{\omega^2 + i\Gamma_D\omega} + \sum_{j=1}^{4} \frac{A_j}{\omega_{0,j}^2 - \omega^2 - i\gamma_j\omega} \tag{1}$$

Here, ε_∞, ω_p, and Γ_D are the background dielectric constant accounting for higher energy interband transitions outside the probed energy spectrum, plasma frequency, and collision frequency, respectively. Four Lorentz oscillators (obtained from Ref. [17–18,25,36]) were used to simulate the interband absorption part of the dielectric function, where peak energy ($\omega_{o,j}$), strength (A_j) and sharpness (γ_j) parameters are obtained by fitting the optical data of the corresponding material. The Lorentz oscillator parameters are listed in Table S1, and these values are fixed for all the W structures reported in this work.

The imaginary part of the dielectric function, ε_2, at long wavelength, where d-band absorption can be neglected, can be written as

$$\varepsilon_2 \approx \frac{\Gamma_D}{\omega} \frac{\omega_p^2}{\omega^2 + \Gamma_D^2} \tag{2}$$

The imaginary part ε_2 is responsible for optical losses in the metal, whereas the real part ε_1 describes the metallicity (free carriers and negative real permittivity) of the metal. The collision frequency term Γ_D is represented by $\Gamma_D = \Gamma_{e\text{-}e} + \Gamma_{e\text{-}p} + \Gamma_{GB} + \Gamma_S$, where $\Gamma_{e\text{-}e}$, $\Gamma_{e\text{-}p}$, Γ_{GB} and Γ_S are the electron–electron scattering involving lattice via umklapp process, electron–phonon scattering, electron grain boundary scattering and electron surface scattering terms, respectively [34,55]. The thickness-dependent parameters of the Drude-Lorentz model are listed in Table S2. The inset in (Fig. 1d) shows that ε_2 increases with decreasing film thickness (from 80 nm to 5 nm) in the visible and near-infrared range and decreases in the mid-infrared range. The variation in Γ_D with respect to d_W is shown in (Fig. 2b). At RT (20 °C), it clearly shows an increment in Γ_D while decreasing d_W down to 5 nm. The variation in Γ_D between 80 nm − 40 nm d_W is marginal, and a large deviation is observed for 10 nm and 5 nm structures. At a fixed temperature, the loss mechanisms responsible for increasing Γ_D with decreasing d_W are Γ_{GB} and Γ_S. The Γ_{GB} is inversely proportional to the grain size and becomes effective when the grain size approaches the electron mean free path of the metal (~15.5 nm for W [56]). It is well known in PC thin film structures that the grain size is reduced when the film thickness is decreased [26,57–58]. The atomic force microscopy (AFM) images of the various d_W structures with grain distributions are shown in (Fig. S3a-e). The RMS roughness of the structures lies between 1 and 1.8 nm; therefore, the influence of the surface roughness on the evaluation of the optical constants was omitted [24,28]. The average grain size of the W structures, as obtained from AFM, with respect to d_W is shown in (Fig. S3f), which clearly depicts an increased grain size with d_W. The W grain size is increased from 11 nm to 85 nm when the d_W changes from 5 nm to 80 nm, and then saturates afterwards, which leads to a 110 nm grain size at 160 nm d_W. During the thin film growth, intrinsic and extrinsic stresses will be generated. According to the Volmer-Weber growth mechanism [59], intrinsic stresses are due to island nucleation

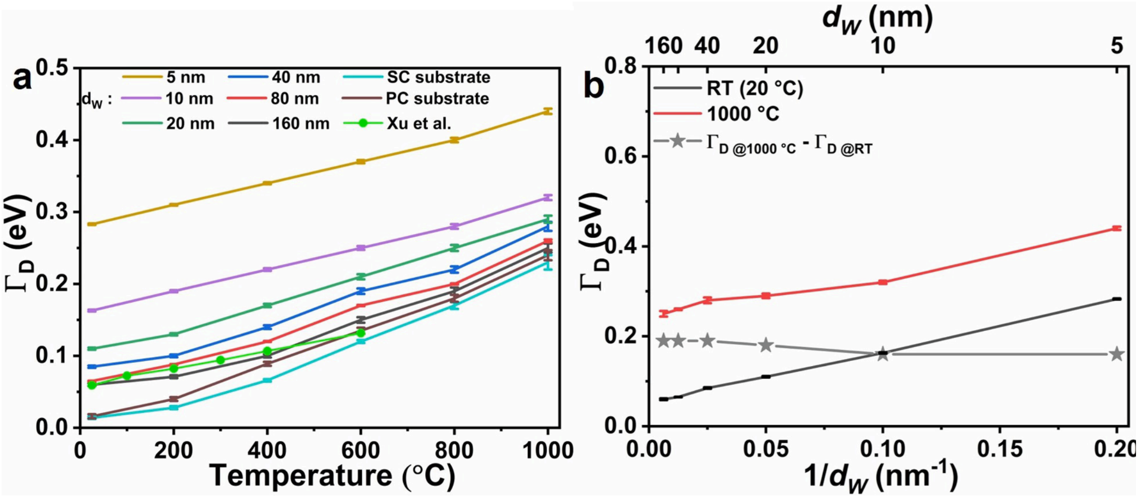

Fig. 2. a) Γ_D as a function of temperature for different film thickness d_W. The error bar designates one standard deviation. The solid lines are a guide to the eye. The green trace shows the data from Xu et al. [18] for a PC W substrate, where Γ_D between RT and 400 °C is extracted from spectroscopic ellipsometer measurements, and the Γ_D at 600 °C is corresponding to the theoretical calculation. b) Γ_D as a function of inverse film thickness d_W at RT and 1000 °C. (For interpretation of the references to colour in this figure legend, the reader is referred to the web version of this article.)

and coalescence, whereas extrinsic stresses are due to the difference in thermal expansion [60]. The stress in the film provides the necessary driving force to the grain growth [61–62], and the relaxation minimizes further growth in the stress, thereby saturating the grain growth. Thus, the grain size is proportional to the film thickness until a saturation thickness is reached [63–67].

Due to the reduced grain size Γ_{GB} will be increased as the film thickness is reduced. W structures with 80 nm and 160 nm d_W (with grain sizes of 85 nm and 110 nm, respectively, Fig. S3) show identical ε_1 and ε_2 values throughout the spectral range (Fig. 1c, 1d), as W films approach bulk like optical properties. At the same time, there is a strong deviation between the PC bulk substrate and the 160 nm film structure, which shows that the bulk properties of thin film sample somehow deviate from the PC bulk sample. The electron-surface scattering contributes to collision frequency in the same way as grain sizes, where the 160 nm d_W structure contains a grain size of 110 nm and the PC bulk substrate contains grains in the range of 10 µm −50 µm.

It should be mentioned that the increase in collision frequency leads to a non-monotonous change of the complex permittivity. In contrast to the visible and near-infrared range, ε_2 in the mid-infrared range decreases as d_W is decreased from 80 nm to 5 nm. The opposite trends at visible to near-infrared and mid-infrared regions can be understood from the following two approximations. Since the Lorentz oscillators represent the interband absorption in the UV–visible range, these terms in Eq (3) and (4) are omitted.

When collision frequency is much smaller than the excitation frequency

$$\Gamma_D \ll \omega, \varepsilon_2 \approx \frac{\omega_p^2 \Gamma_D}{\omega^3}; \tag{3}$$

ε_2 increases with collision frequency in the visible and near-infrared region, whereas, when

$$\Gamma_D \gg \omega, \varepsilon_2 \approx \frac{\omega_p^2}{\omega \Gamma_D}; \tag{4}$$

ε_2 decreases with increasing the Γ_D in the mid-infrared region (above 6000 nm wavelength). Further, a continuous decrement in the absolute value of the negative ε_1 (Fig. 1c) is observed throughout the spectral range when d_W decreases, i.e., from 80 nm to 5 nm. It indicates that the metallicity of the W film is reduced when the film thickness is decreased. Fig. 1c shows that the change in ε_1 is minimal around visible to near-infrared regions, and significant at mid-infrared wavelengths. This can be explained with the following expressions:

When $\Gamma_D \ll \omega$, ε_1 is mainly described by

$$\varepsilon_1 \approx \frac{-\omega_p^2}{\omega^2} \tag{5}$$

i.e., ε_1 is not regulated by Γ_D, and ε_1 is associated with ω_p. This will be true for most of the metals in the visible and near-infrared range. However, when Γ_D is comparable to or larger than ω,

$$\varepsilon_1 = \frac{-\omega_p^2}{\omega^2 + \Gamma_D^2}. \tag{6}$$

Thus, ε_1 depends on Γ_D at longer wavelengths. In the mid-infrared regions above 6000 nm wavelengths, a large difference in the magnitude of ε_1 (580 and 2370 at 6000 nm and 12000 nm, respectively) is observed when d_W is reduced from 80 nm to 5 nm, which is due to increase in Γ_D. The qualitative behaviour of ε_1 as predicted by equation (6) is clearly visible in the Fig. 3. For instance, 160 nm thick film at 1000 °C shows ε_1 values that saturate towards mid-infrared wavelengths, therefore ε_1 becomes almost independent of the ω.

Further, to compare the optical properties of W thin films with bulk W substrates, SC and PC bulk W substrates were investigated. The SC W substrate shows the lowest values for ε_1 and ε_2 compared to the PC substrate and other W thin film (160 nm- 5 nm) structures (Fig. 1c, 1d). Since the SC substrate is free from any grain boundaries, the optical losses are expected to be minimum in SC W substrate, and the contributions of Γ_{GB} are zero. On the other hand, there might still be a contribution from Γ_S as ellipsometry measures reflected light that also excites electrons close to the surface. Despite a low surface roughness of PC W substrate comparable to SC W substrate, 0.8 nm vs 0.5 nm, respectively (Fig. S4), the PC W substrate shows a slight deviation in ε_1 and ε_2 compared to SC W substrate at wavelengths higher than 6000 nm (Fig. 1c, 1d). Which can be described by a slight increase in the collision frequency of the PC W substrate. The PC W substrate contains grains in the range of 10 µm −50 µm, which should not contribute to a measurable difference in collision frequency. This difference is probably an artefact due to the imperfections or dislocations in the PC W substrate, which is attributed by the ellipsometric fitting to change of permittivity of the film. PC substrate shows a good agreement with the permittivity values reported by Xu et al [18]. For example, in this work, ε_2 of 20 and 791 were observed at 1000 nm and 12000 nm, respectively, whereas in Xu et al. [18] work, 17 and 1025 were observed at the corresponding wavelengths. The observed differences in the permittivity values are due

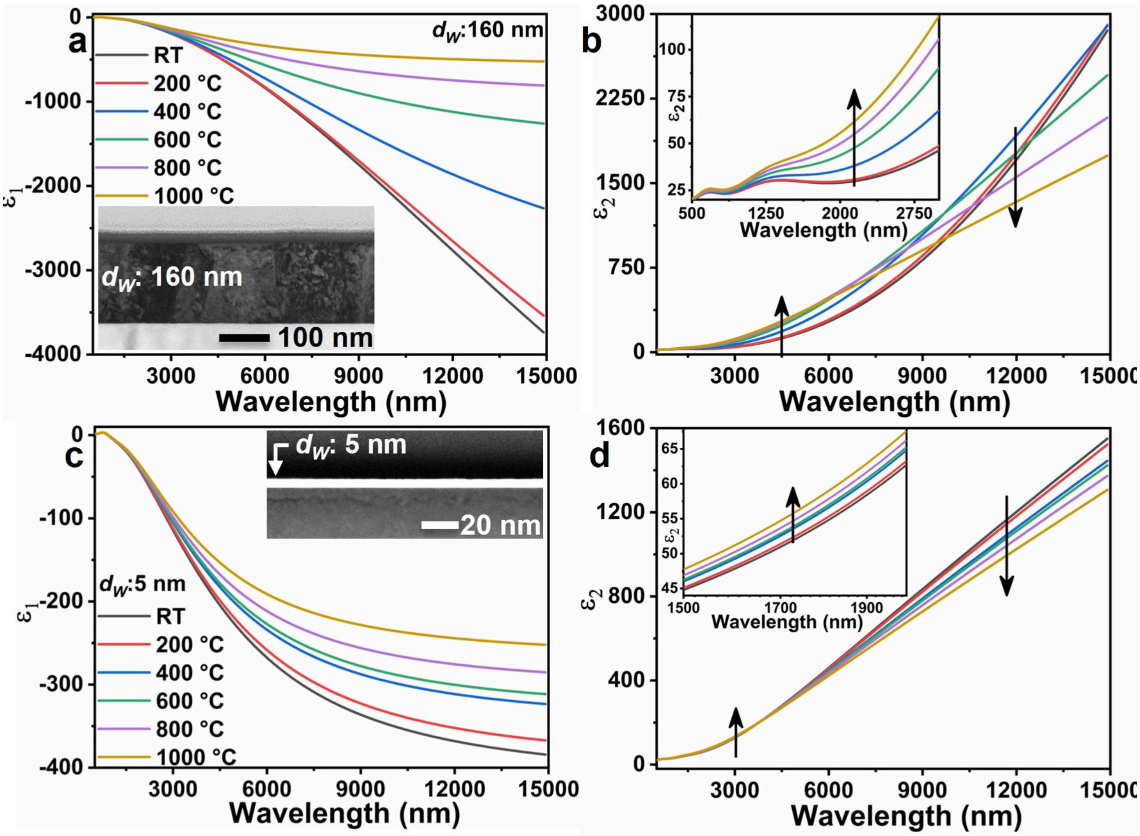

Fig. 3. a, b) In-situ real and complex dielectric permittivities, ε_1 and ε_2, respectively, of a 160 nm d_W structure at RT, and high temperatures, up to 1000 °C under 2 × 10^{-5} mbar vacuum pressure. Similarly, in-situ real and complex dielectric permittivities of a 5 nm d_W structure are shown in (c, d). As-fabricated BF-TEM images of 160 nm and 5 nm W structures are shown in the insets of (a and c), respectively.

to the structural differences between the PC substrates.

In order to investigate the effect of the temperature on the optical constants, W film structures with various d_W were investigated at high temperatures using an in-situ spectroscopic ellipsometer. W is prone to oxidization at 1000 °C when there is no protective layer, or enough residual O_2 partial pressure is available in the heating chamber [10,51]. Herein, the heating chamber is operated under a high vacuum, thereby, no oxidization of W is expected. The oxidization behaviour of W at different vacuum conditions is investigated, and discussed in the Supporting Information (Fig. S5).

Fig. 3 shows ε_1 and ε_2 of the W structures with 160 nm and 5 nm thicknesses at RT and high temperatures up to 1000 °C, and the corresponding as-fabricated bright-field (BF) TEM images are shown in the insets of Fig. 3a, 3c. Optical constants for all d_W in the visible-mid infrared range are shown in Fig. S6 and S7, and in the visible to near-infrared range are shown in Fig. S8 and S9. As it can be seen in (Fig. 3b), for a 160 nm d_W, ε_2 increases in the visible and near-infrared range, and it decreases in the mid-infrared range. (Fig. 2a) shows that for a 160 nm d_W, an increment in Γ_D is observed with respect to temperature. The temperature-dependent Γ_D term is given by $\Gamma_{e\text{-}e}$ and $\Gamma_{e\text{-}p}$, where Γ_D is connected to scattering rate τ as $\Gamma_D = \hbar/\tau$, with ħ as the reduced Planck constant. According to the Born approximation and Thomas-Fermi screening of the Coulomb interaction [68–70],

$$\frac{1}{\tau_{e-e}} = \frac{1}{12}\pi^3\Gamma\Delta\frac{1}{\hbar E_F}\left[(k_BT)^2 + \left(\frac{\hbar\omega}{2\pi}\right)^2\right] \tag{7}$$

Here, Γ, Δ, E_F and k_B are the average scattering probability, the fractional Umklapp scattering, Fermi energy of the free electrons and Boltzmann constant, respectively. From Eq. (7), $\Gamma_{e\text{-}e}$ depends on temperature and frequency. However, the term $(k_BT)^2$ is smaller than $\left(\frac{\hbar\omega}{2\pi}\right)^2$ for all the temperatures and frequencies used in this study. Therefore, the contribution of $\Gamma_{e\text{-}e}$ with respect to temperature is not considered. According to the electron–phonon gas theory of Holstein [71–73], the electron–phonon scattering rate defining the electron–phonon scattering frequency is given by

$$\frac{1}{\tau_{e-p}} = \frac{1}{\tau_0}\left[\frac{2}{5} + \frac{T}{\theta}\right] \tag{8}$$

where θ is the Debye temperature. It clearly shows that Γ_{e-p} increases linearly at large temperatures. When the temperature of the metal is raised, the mean phonon number density in the metal will increase according to Bose-Einstein statistics, which enhances the electron–phonon scattering. (Fig. 2a) shows Γ_D vs T for different d_W. A linear relationship is observed between Γ_D and T, regardless of d_W. Xu et al. [18] show the measured and calculated temperature-dependent optical properties of PC W substrate at temperatures up to 400 °C and 600 °C, respectively, (Fig. 2a-green trace), where a monotonic increment in the Γ_D is clearly observed with a rise in the temperature. The Γ_D of the PC W substrate changes from 0.059 eV to 0.11 eV when the temperature rises from RT to 400 °C, whereas in the current work it varies from 0.02 eV to 0.09 eV. The rate of Γ_D change with respect to temperature is 0.13 meV/°C and 0.18 meV/°C, in Xu et al. [18] and the current work, respectively. A good agreement is observed for Γ_D at 600 °C. The difference in Γ_D at RT between Xu et al. [18] and the current work can be attributed to the structural properties of the PC W substrate, where the impurities, grain size, surface roughness and oxidization determine the Γ_D.

Fig. 2b shows the variation of Γ_D vs $1/d_W$ at RT and 1000 °C, where the two traces are parallel to each other. It is clearly seen that $\Gamma_{D@1000\,°C}$ -$\Gamma_{D@RT}$ is approximately a constant (Fig. 2b-gray trace) for every d_W. Similarly, for other temperatures, $\Gamma_{D@HT}$ -$\Gamma_{D@RT}$ is always a constant (from the linear Γ_D vs T, Fig. 2a). Thus, it can be concluded that Γ_{e-p}

does not depend on film thickness. In summary, Γ_D increases linearly with temperature due to Γ_{e-p}, and inversely proportional to d_W due to Γ_{GB} and Γ_S. The temperature-dependent parameters of the Drude-Lorentz model of 160 nm d_W film thickness are shown in Table S3 and Fig. S10. The standard deviation of the Γ_D lies between 0.9 meV and 3.1 meV when the temperature of 160 nm d_W structure is raised from RT to 1000 °C, respectively, which account for a minimal change of 1.2% of Γ_D at 1000 °C. The observed ε_2 trends in different spectral regions (Fig. 3b) can be explained using Eqs. (3) and (4): When $\Gamma_D \ll \omega$, ε_2 increases with temperature, and when $\Gamma_D \gg \omega$, ε_2 decreases with the temperature. Similarly, the 5 nm W structure also shows different ε_2 tendencies in the different spectral ranges (Fig. 3d).

Fig. 3a,c shows the temperature-dependent ε_1 of 160 nm and 5 nm d_W. A positive change of ε_1 is observed when the temperature is raised from RT to 1000 °C. At high temperatures, the changes in ε_1 are primarily associated with Γ_D. Additional contribution can be expected from a change of ω_p. The plasma frequency is given by,

$$\omega_p = \sqrt{\frac{Ne^2}{m^* \epsilon_0}} \tag{9}$$

Here N, e, m^* and ϵ_0 are the free-electron carrier density, charge of the electron, electron effective mass and free space permittivity. As the temperature is raised, due to lattice thermal expansion, N will be slightly reduced and thereby decrease the plasma frequency. On the other hand, the effective mass may increase or decrease in different metals [74]. Thus, the interplay between N and m^* defines ω_p. These parameters can be different, depending on the growth and quality of the deposited films. A non-monotonic behaviour of ω_p (Fig. S10) is observed for a 160 nm d_W structure, similar to other metals at high temperatures, such as Au, Ag, TiN, etc [29,33,41]. From Table S2, ω_p changes only slightly with temperature and as the maximum deviation observed between RT and 1000 °C is around 6%, thus, no significant changes in the optical properties are expected. Moreover, the standard deviation of ω_p is less than 1% for the entire measured temperature range. Fig. S11 shows the effect of including roughness in the ellipsometric model of the optical constants for a 160 nm d_W structure, where no variation in the optical constants was observed. Thus, the roughness has a negligible effect on ω_p and Γ_D. Therefore, the observed changes in ε_1 at high temperatures is primarily due to Γ_D (Eq. (5) and (6)).

The SC and PC W substrates also show similar trends for ε_1 and ε_2 (Fig. S12) at high temperatures. In the Xu et al. work [18], the calculated ω_p of the PC W substrate at RT from theoretical calculations and spectroscopic ellipsometry measurements is 7.13 eV and 5.21 eV, respectively, and a variation between 5.85 eV and 7.81 eV is reported elsewhere [17,75–77]. Whereas in the current work, the PC W substrate exhibits a ω_p of 6 eV. Xu et al. [18] show a linear decrement in ω_p when the temperature is increased from RT to 400 °C, whereas in the current work a non-monotonic change in ω_p is observed (Table S4).

To assess the structural modifications in the film structures after measuring the optical constants at high temperatures, transmission electron microscopy (TEM) investigations were performed. Fig. S13 shows the BF-TEM images of 5 nm and 160 nm d_W structures before and after measuring the optical constants using in-situ ellipsometry at temperatures up to 1000 °C, under a high vacuum condition of 2×10^{-5} mbar pressure. Since the W films were optimized to grow in α-W, which is thermodynamically stable, minimum structural changes can be expected after heating the W structures at high temperatures. As seen in Fig. S14, the X-ray reflection of the α-W at (110) is left intact, and no sign of β-W or W-oxides are observed after heating the 160 nm structure at 1000 °C. Further, a narrow reflection (110) of the heated structure confirms the grain growth in the W structure owing to the thermal activation processes. Still, W thin films show unprecedented thin film stability without island formation after the heat treatment at 1000 °C. The 160 nm d_W structure is left intact compared to the as-fabricated structure, and even the 5 nm structure shows a continuous layer of W film without any breakage (Fig. S13b). It is noted that defects such as pinholes or voids are not observed after heating the W structures at 1000 °C. The RMS roughness of the W structures remains below 1.8 nm, which is consistent with the reported data [49,78].

Fig. 4a-d show scanning transmission electron microscopy high-angle annular dark-field (STEM-HAADF) images and element maps created by EDS analyses of the as-fabricated 5 nm d_W structure. Similarly, for a 160 nm d_W structure, the spectrum images are shown in (Fig. 4f-h). The elements W, O and Al can be seen in the spectrum images, and the as-fabricated W structures are free from any O_2 contamination during the deposition process. Fig. 4i-l and 4m-p show the STEM-HAADF and spectral images of the 5 nm and 160 nm d_W structures, respectively, after heating at 1000 °C. There is no evidence of O observed in the W structures due to the small residual partial O_2 pressure in the heating chamber (Fig. 4k,o). The magnified areas of the W structures around the Al_2O_3 interface, marked on Fig. 4i,m, are shown in (Fig. 4q-x and S15). No inter-diffusion of W into the Al_2O_3 layer or vice-versa is observed in the 5 nm and 160 nm d_W structures, whereas the 5 nm d_W structure shows W content at the Al_2O_3 interface. From the EDS intensity profiles shown in Fig. S16, the W droplets at the W/Al_2O_3 are likely due to the redeposition of W residues during the FIB Lamella preparation.

The long-term thermal stability of the W thin film is investigated by annealing an 80 nm d_W structure at 1000 °C up to 120 h under a high vacuum condition of 2×10^{-6} mbar pressure (Fig. S17). W structures show exceptional thermal stability when the partial O_2 pressure in the annealing chamber is low [10,79].

Further, to demonstrate the application of film thickness and temperature-dependent optical properties of W, a hyperbolic metamaterial emitter (based on W and HfO_2) is designed and fabricated as a spectrally selective thermal emitter for TPV application [8,10,79]. In TPV, the emitter should provide a step-shaped spectral response to match the external quantum efficiency of the PV cell. Therefore, a selective thermal emitter should provide an emissivity $\varepsilon = 1$ for $E > E_g$ and $\varepsilon = 0$ for $E < E_g$, where E and E_g are the thermal photon energy and bandgap energy of the PV cell, respectively. A schematic presentation of the W and HfO_2-based 1D hyperbolic multi-layered metamaterial emitter is shown in the inset of (Fig. 5a), where six bilayers of W and HfO_2, with thicknesses of 20 nm and 100 nm, respectively, are sandwiched between a bottom thick W layer and a top protective HfO_2 layer, each of 100 nm thickness. These thicknesses were chosen in order to adjust the cutoff wavelength to an InGaAsSb PV cell with a bandgap of $E_g = 0.55$ eV ($\triangleq$ 2.25 μm) [80], which corresponds to the blackbody maximum of the emitter at 1000 °C. The calculated and measured absorptivity of the emitter are shown in (Fig. 5a). This is equivalent to emissivity due to Kirchoff's law. A transfer matrix method (TMM) is used to calculate the absorptivity spectrum. For example, when the bulk W substrate optical constants were used to model both thin and thick (20 nm and 100 nm, respectively) d_W films in the metamaterial structure, the calculated spectrum (Fig. 5a-solid cyan line) shows a shallow decrease in the absorptivities/emissivities around 2 μm spectral region. Particularly in the near-infrared regions, the absorptivity/emissivity goes below 5%, and it appears to be an ideal structure to use in TPV. However, the measured absorptivity/emissivity spectrum (Fig. 5a-black dotted line) shows a good correspondence with the calculated spectrum below 1.7 μm and afterwards, a significant deviation (relatively a 2–5 × increment) in the absorptivity/emissivity is observed at the near-infrared region. Thus, if the bulk optical constants were used to model the structure, a substantial difference in the spectral efficiency can be expected. Similarly, in the other works published elsewhere [2,8,20–22], drastic variations between the calculated and measured optical spectra are observed. Whereas, when the thin film optical constants measured by the ellipsometer are used in the TMM calculations, (the optical constants of 20 nm and 80 nm d_W structures measured at RT-Fig. 1c,1d), Fig. 5a-solid black line shows the obtained absorptivity/

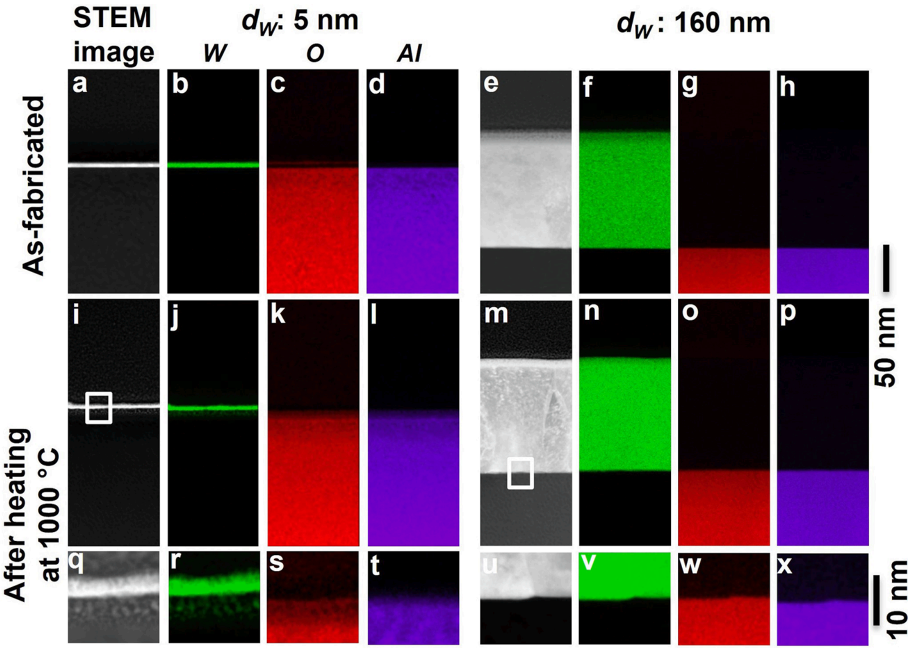

Fig. 4. a-d) STEM-HAADF image of as-fabricated 5 nm d_W structure (a), and elemental mapping images (b-d) showing the distribution of W, O and Al. Similarly, a 160 nm d_W structure is shown in (e-h). STEM-HAADF images (i, m) and element maps (j-l and n-p) of the W structures with 5 and 160 nm d_W after heating at 1000 °C under 2×10^{-5} mbar vacuum pressure. q-x) Magnified views of the marked areas on (i and m) and their corresponding element maps.

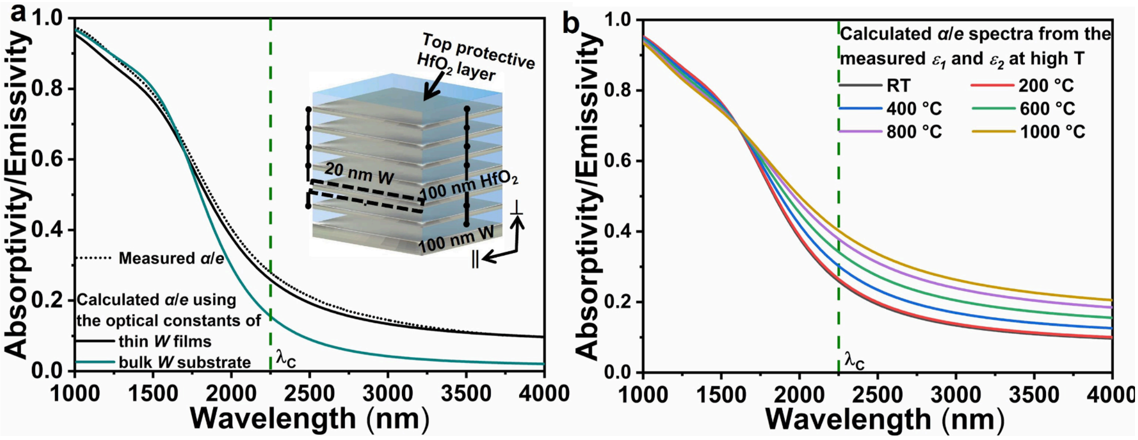

Fig. 5. a) Calculated and measured absorptivity or emissivity (α/e) of a hyperbolic metamaterial emitter structure at RT. λ_C is the cut-off wavelength of the PV cell. The insert shows the geometry of the structure. b) The calculated absorptivity/emissivity of the structure at high temperatures, up to 1000 °C, calculated from the optical constants measured using an in-situ high temperature ellipsometer.

emissivity spectrum. Since there is no difference between the optical constants of 80 nm and 160 nm d_W structures (Fig. 1c,1d), an 80 nm d_W structure optical data is used in TMM calculations to model the 100 nm thick bottom layer of the metamaterial structure. The calculated absorptivity/emissivity spectrum shows a good spectral match (~95%) with the measured spectrum, where minute differences might be attributed to the measurement technique (see the experimental section). Therefore, it is pivotal to use the optical constants of the appropriate thin film structures in the model to calculate/estimate the optical functionality of the structures precisely.

Furthermore, a significant increase in the collision frequency is expected at elevated temperatures, thereby changing the spectral selectivity of the emitter. Fig. 5b shows the calculated absorptivity/emissivity spectra of the 1D metamaterial emitter at RT and high temperatures, up to 1000 °C, where the optical constants of the 20 nm and 80 nm d_W structures measured using an in-situ spectroscopic ellipsometer at the respective temperatures (Fig. S6 and S7) are used. As can be seen in Fig. 5b, the spectral emissivity at the long-wavelength region (above the cutoff wavelength λ_C of the PV cell) increases with temperature due to *e-p* scattering. A marginal increment in the emissivity is noticed at 200 °C, and thereafter a significant increment in the emissivity is observed starting from 400 °C. At 1000 °C, an average of more than 2 × increment in the emissivity is observed at longer wavelengths. The spectral efficiency of the emitter, $\eta_{emitter}$, is calculated using Eq. (10).

$$\eta_{emitter} = \int_{E_g}^{\infty} \frac{E_g}{E}\varepsilon(E) I_{BB}(E, T_{emitter}) dE \Big/ \int_{0}^{\infty} \varepsilon(E) I_{BB}(E, T_{emitter}) dE \quad (10)$$

where ε, $T_{emitter}$, and I_{BB} correspond to the spectral emissivity, emitter temperature and blackbody spectral power density at the emitter temperature, respectively. At 1000 °C, the 1D metamaterial emitter exhibits $\eta_{emitter} \sim 34\%$ in comparison to 19% which will be obtained with just the black body emission. For instance, when there is no increment in the emissivity at longer wavelengths during the high temperature operation of 1000 °C, i.e., using the RT optical constants of W thin film structures at high temperatures, 1D emitter exhibits $\eta_{emitter} \sim 44\%$. However, when the RT bulk W data is used, the emitter spectral efficiency is overestimated to 58%. Thus, a substantial change in the perceived spectral efficiency is observed when the RT optical constants are used to calculate the optical properties of the structures at high temperatures. In order to obtain realistic values, therefore, it is crucial to use the high temperature optical constants of the thin film structures to calculate the optical properties of the nanostructures at elevated temperatures.

4. Conclusion

The optical properties of W thin films with thicknesses between 5 nm −160 nm in the wavelength range of 500 nm – 15000 nm are investigated in the temperature range from room temperature up to 1000 °C. By decreasing the W film thickness below 80 nm, an increased imaginary part of the complex-dielectric permittivity is observed. Once the film thickness or grain size approaches the length scales of the electron mean free path, the optical constants of the films change drastically due to additional electron scattering, where the additional collision frequency is inversely proportional to d_W.

At high temperatures, the increase in phonon density causes a large *e-p* scattering which is proportional to the temperature change and further increases the optical losses in the structure. The electron–phonon interaction becomes the dominant loss mechanism at high temperatures, even in thin film structures.

The significance of the film thickness and temperature-dependent optical constants of the W structures in high temperature applications is demonstrated with an example of a 1D hyperbolic metamaterial emitter structure. When the bulk optical constants are used to model the structures, a substantial deviation between calculated and measured absorptivity/emissivity spectra are observed. Whereas, when the optical constants of thin films are used, the calculated and measured absorptivity/emissivity spectra show a good agreement, which highlights the accuracy of the optical constants evaluated from thin films. These findings underline the necessity of the thickness and temperature-dependent optical constants of the thin films to accurately model and optimize the optical properties of the photonic/plasmonic nanostructures at RT and elevated temperatures.

CRediT authorship contribution statement

Mahima Arya: Writing the manuscript, Ellipsometer measurements, reflection measurements and thermal stability measurements. **Ankita Ganguly:** Ellipsometer measurements, reflection measurements and thermal stability measurements. **Gnanavel V. Krishnamurthy:** Fabrication of W structures, performed XRD measurements and analyzed the diffraction patterns considering phase formation and structural properties. **Surya S. Rout:** STEM-imaging and elemental mapping,. **Leonid Gurevich:** AFM imaging and analysis. **Tobias Krekeler:** STEM-imaging and elemental mapping. **Martin Ritter:** STEM-imaging and elemental mapping. **Kjeld Pedersen:** Conceptualization, reviewing and editing the manuscript. **Michael Störmer:** Fabrication of W structures, performed XRD measurements and analyzed the diffraction patterns considering phase formation and structural properties. **Alexander Yu Petrov:** Conceptualization, reviewing and editing the manuscript. **Manfred Eich:** Conceptualization, reviewing and editing the manuscript. **Manohar Chirumamilla:** Conceptualization, Writing – review & editing, Writing the manuscript, Ellipsometer measurements, reflection measurements and thermal stability measurements, reviewing and editing the manuscript.

Declaration of Competing Interest

The authors declare that they have no known competing financial interests or personal relationships that could have appeared to influence the work reported in this paper.

Acknowledgements

The authors gratefully acknowledge financial support from the German Research Foundation (DFG) via SFB 986 ‘Tailor-Made Multi-Scale Materials Systems: M3’, Project-ID 192346071, and projects C1, C7 and Z3. K. Pedersen acknowledges the financial support from the Novo Nordisk, grant number NNF20OC0064735.

Appendix A. Supplementary material

Supplementary data to this article can be found online at https://doi.org/10.1016/j.apsusc.2022.152927.

References

[1] M. Chirumamilla, A.S. Roberts, F. Ding, D. Wang, P.K. Kristensen, S.I. Bozhevolnyi, K. Pedersen, Multilayer tungsten-alumina-based broadband light absorbers for high-temperature applications, Opt. Mater. Express 6 (2016) 2704.
[2] K. Cui, P. Lemaire, H. Zhao, T. Savas, G. Parsons, A.J. Hart, Tungsten-Carbon Nanotube Composite Photonic Crystals as Thermally Stable Spectral-Selective Absorbers and Emitters for Thermophotovoltaics, Adv. Energy Mater. 8 (2018) 1801471.
[3] E. Brodu, M. Balat-Pichelin, J.L. Sans, J.C. Kasper, Evolution of the emissivity of tungsten at high temperature with and without proton bombardment, Acta Mater. 84 (2015) 305.
[4] R. Freeman, F. Rigby, S. Doerr, L. Grimes, D. Ward, Reflectance of laser-damaged spacecraft thermal control materials, Proc. SPIE 3343 (1998) 983.
[5] O. Ilic, P. Bermel, G. Chen, J.D. Joannopoulos, I. Celanovic, M. Soljačić, Tailoring high-temperature radiation and the resurrection of the incandescent source, Nat. Nanotechnol. 11 (2016) 320.
[6] J.H. Park, S.E. Han, P. Nagpal, D.J. Norris, Observation of Thermal Beaming from Tungsten and Molybdenum Bull’s Eyes, ACS Photonics 3 (2016) 494.
[7] D. Shin, G. Kang, P. Gupta, S. Behera, H. Lee, A.M. Urbas, W. Park, K. Kim, Thermoplasmonic and Photothermal Metamaterials for Solar Energy Applications, Adv. Opt. Mater. 6 (2018) 1800317.
[8] P.N. Dyachenko, S. Molesky, A.Y. Petrov, M. Störmer, T. Krekeler, S. Lang, M. Ritter, Z. Jacob, M. Eich, Controlling thermal emission with refractory epsilon-near-zero metamaterials via topological transitions, Nat. Commun. 7 (2016) 11809.
[9] A. Lenert, D.M. Bierman, Y. Nam, W.R. Chan, I. Celanović, M. Soljačić, E.N. Wang, A nanophotonic solar thermophotovoltaic device, Nat. Nanotechnol. 9 (2014) 126.
[10] M. Chirumamilla, G.V. Krishnamurthy, K. Knopp, T. Krekeler, M. Graf, D. Jalas, M. Ritter, M. Störmer, A.Y. Petrov, M. Eich, Metamaterial emitter for thermophotovoltaics stable up to 1400 °C, Sci. Rep. 9 (2019) 7241.
[11] L. Boltzmann, Ableitung des Stefan’schen Gesetzes, betreffend die Abhängigkeit der Wärmestrahlung von der Temperatur aus der electromagnetischen Lichttheorie, Ann. Phys. 258 (1884) 291.
[12] J. Stefan, über die Beziehung zwischen der Wärmestrahlung und der Temperatur, Sitzungsberichte der Kaiserlichen Akademie der Wissenschaften in Wien 79 (1879) 391.
[13] S. Gharibzadeh, B. Abdollahi Nejand, M. Jakoby, T. Abzieher, D. Hauschild, S. Moghadamzadeh, J.A. Schwenzer, P. Brenner, R. Schmager, A.A. Haghighirad, L. Weinhardt, U. Lemmer, B.S. Richards, I.A. Howard, U.W. Paetzold, Record Open-Circuit Voltage Wide-Bandgap Perovskite Solar Cells Utilizing 2D/3D Perovskite Heterostructure, Adv. Energy Mater. 9 (2019) 1803699.
[14] D.M. Bierman, A. Lenert, W.R. Chan, B. Bhatia, I. Celanović, M. Soljačić, E. N. Wang, Enhanced photovoltaic energy conversion using thermally based spectral shaping, Nat. Energy 1 (2016) 16068.
[15] D. W. Lynch, W. R. Hunter, in *Handbook of Optical Constants of Solids* (Ed: E. D. Palik), Academic Press, Burlington 1997, p. 275.
[16] J.H. Weaver, C.G. Olson, D.W. Lynch, Optical properties of crystalline tungsten, Phys. Rev. B 12 (1975) 1293.
[17] A.D. Rakić, A.B. Djurišić, J.M. Elazar, M.L. Majewski, Optical properties of metallic films for vertical-cavity optoelectronic devices, Appl. Opt. 37 (1998) 5271.
[18] M. Xu, J.-Y. Yang, L. Liu, Temperature-dependent dielectric functions of bcc transition metals Cr, Mo, and W from ultraviolet to infrared regions: A theoretical and experimental study, J. Appl. Phys. 123 (2018), 155102.
[19] P.B. Johnson, R.W. Christy, Optical Constants of the Noble Metals, Phys. Rev. B 6 (1972) 4370.
[20] J.H. Kim, S.M. Jung, M.W. Shin, Thermal degradation of refractory layered metamaterial for thermophotovoltaic emitter under high vacuum condition, Opt. Express 27 (2019) 3039.
[21] C.-C. Chang, W.J.M. Kort-Kamp, J. Nogan, T.S. Luk, A.K. Azad, A.J. Taylor, D.A. R. Dalvit, M. Sykora, H.-T. Chen, High-Temperature Refractory Metasurfaces for Solar Thermophotovoltaic Energy Harvesting, Nano Lett. 18 (2018) 7665.
[22] N. Jeon, J.J. Hernandez, D. Rosenmann, S.K. Gray, A.B.F. Martinson, J.J. Foley, Pareto Optimal Spectrally Selective Emitters for Thermophotovoltaics via Weak Absorber Critical Coupling, Adv. Energy Mater. 8 (2018) 1801035.

[23] J.H. Kim, S.M. Jung, M.W. Shin, High-temperature degradation of one-dimensional metallodielectric (W/SiO2) photonic crystal as selective thermal emitter for thermophotovoltaic system, Opt. Mater. 72 (2017) 45.

[24] K.M. McPeak, S.V. Jayanti, S.J.P. Kress, S. Meyer, S. Iotti, A. Rossinelli, D.J. Norris, Plasmonic Films Can Easily Be Better: rules and Recipes, ACS Photonics 2 (3) (2015) 326–333.

[25] K.C. Maurya, B. Biswas, D. Rao, B. Saha, Giant enhancement of plasmonic response and epsilon-near-zero signature in refractory transition metals (Ta, W, and Mo) deposited at high-temperature, Appl. Phys. Lett. 118 (2021), 041902.

[26] G. Ding, C. Clavero, D. Schweigert, M. Le, Thickness and microstructure effects in the optical and electrical properties of silver thin films, AIP Adv. 5 (2015), 117234.

[27] D.I. Yakubovsky, A.V. Arsenin, Y.V. Stebunov, D.Y. Fedyanin, V.S. Volkov, Optical constants and structural properties of thin gold films, Opt. Express 25 (2017) 25574.

[28] J.H. Park, P. Ambwani, M. Manno, N.C. Lindquist, P. Nagpal, S.-H. Oh, C. Leighton, D.J. Norris, Single-Crystalline Silver Films for Plasmonics, Adv. Mater. 24 (2012) 3988.

[29] H. Reddy, U. Guler, K. Chaudhuri, A. Dutta, A.V. Kildishev, V.M. Shalaev, A. Boltasseva, Temperature-Dependent Optical Properties of Single Crystalline and Polycrystalline Silver Thin Films, ACS Photonics 4 (2017) 1083.

[30] N.A. Pfiester, K.A. Grossklaus, M.A. Stevens, T.E. Vandervelde, Effect of microstructure on the optical properties of sputtered iridium thin films, Opt. Mater. Express 10 (2020) 1120.

[31] L. Ciambriello, E. Cavaliere, L. Gavioli, Influence of roughness, porosity and grain morphology on the optical properties of ultrathin Ag films, Appl. Surf. Sci. 576 (2022), 151885.

[32] J. Kim, H. Oh, B. Kang, J. Hong, J.-J. Rha, M. Lee, Broadband Visible and Near-Infrared Absorbers Implemented with Planar Nanolayered Stacks, ACS Appl. Nano Mater. 3 (2020) 2978.

[33] H. Reddy, U. Guler, A.V. Kildishev, A. Boltasseva, V.M. Shalaev, Temperature-dependent optical properties of gold thin films, Opt. Mater. Express 6 (2016) 2776.

[34] J. Sotelo, J. Ederth, G. Niklasson, Optical properties of polycrystalline metallic films, Phys. Rev. B 67 (2003), 195106.

[35] D.I. Yakubovsky, R.V. Kirtaev, Y.S. Stebunov, A.V. Arsenin, V.S. Volkov, Morphology and effective dielectric functions of ultra-thin gold films, J. Phys. Conf. Ser. 1092 (2018), 012167.

[36] M.P. Wells, R. Bower, R. Kilmurray, B. Zou, A.P. Mihai, G. Gobalakrichenane, N. M. Alford, R.F.M. Oulton, L.F. Cohen, S.A. Maier, A.V. Zayats, P.K. Petrov, Temperature stability of thin film refractory plasmonic materials, Opt. Express 26 (2018) 15726.

[37] J.I. Watjen, T.J. Bright, Z.M. Zhang, C. Muratore, A.A. Voevodin, Spectral radiative properties of tungsten thin films in the infrared, Int. J. Heat Mass Transf. 61 (2013) 106.

[38] M. Minissale, C. Pardanaud, R. Bisson, L. Gallais, The temperature dependence of optical properties of tungsten in the visible and near-infrared domains: an experimental and theoretical study, J. Phys. D: Appl. Phys. 50 (2017), 455601.

[39] A. Chirumamilla, Y. Yang, M.H. Salazar, F. Ding, D. Wang, P.K. Kristensen, P. Fojan, S.I. Bozhevolnyi, D.S. Sutherland, K. Pedersen, M. Chirumamilla, Spectrally selective emitters based on 3D Mo nanopillars for thermophotovoltaic energy harvesting, Mater. Today Phys. 21 (2021), 100503.

[40] T. Krekeler, S.S. Rout, G.V. Krishnamurthy, M. Störmer, M. Arya, A. Ganguly, D. S. Sutherland, S.I. Bozhevolnyi, M. Ritter, K. Pedersen, A.Y. Petrov, M. Eich, M. Chirumamilla, Unprecedented Thermal Stability of Plasmonic Titanium Nitride Films up to 1400 °C, Adv. Opt. Mater. 9 (2021) 2100323.

[41] H. Reddy, U. Guler, Z. Kudyshev, A.V. Kildishev, V.M. Shalaev, A. Boltasseva, Temperature-Dependent Optical Properties of Plasmonic Titanium Nitride Thin Films, ACS Photonics 4 (2017) 1413.

[42] J.A. Briggs, G.V. Naik, T.A. Petach, B.K. Baum, D. Goldhaber-Gordon, J.A. Dionne, Fully CMOS-compatible titanium nitride nanoantennas, Appl. Phys. Lett. 108 (2016), 051110.

[43] R. Henriquez, L. Moraga, G. Kremer, M. Flores, A. Espinosa, R.C. Munoz, Size effects in thin gold films: Discrimination between electron-surface and electron-grain boundary scattering by measuring the Hall effect at 4 K, Appl. Phys. Lett. 102 (2013), 051608.

[44] E.-T. Hu, Q.-Y. Cai, R.-J. Zhang, Y.-F. Wei, W.-C. Zhou, S.-Y. Wang, Y.-X. Zheng, W. Wei, L.-Y. Chen, Effective method to study the thickness-dependent dielectric functions of nanometal thin film, Opt. Lett. 41 (2016) 4907.

[45] Y.F. Zhu, X.Y. Lang, W.T. Zheng, Q. Jiang, Electron Scattering and Electrical Conductance in Polycrystalline Metallic Films and Wires: impact of Grain Boundary Scattering Related to Melting Point, ACS Nano 4 (2010) 3781.

[46] E.D. Palik, Handbook of the Optical Constants of Solids, Academic Press, San Diego, CA, 1988.

[47] T. Smith, Optical Constants of Clean Titanium and Tungsten Surfaces as Functions of Temperature, J. Opt. Soc. Am. 62 (1972) 774.

[48] F.T.N. Vüllers, R. Spolenak, Alpha- vs. beta-W nanocrystalline thin films: A comprehensive study of sputter parameters and resulting materials' properties, Thin Solid Films 577 (2015) 26.

[49] K. Salamon, O. Milat, N. Radić, P. Dubček, M. Jerčinović, S. Bernstorff, Structure and morphology of magnetron sputtered W films studied by x-ray methods, J. Phys. D: Appl. Phys. 46 (2013), 095304.

[50] G.V. Krishnamurthy, M. Chirumamilla, S.S. Rout, K.P. Furlan, T. Krekeler, M. Ritter, H.-W. Becker, A.Y. Petrov, M. Eich, M. Störmer, Structural degradation of tungsten sandwiched in hafnia layers determined by in-situ XRD up to 1520 °C, Sci. Rep. 11 (2021) 3330.

[51] S.C. Cifuentes, M.A. Monge, P. Pérez, On the oxidation mechanism of pure tungsten in the temperature range 600–800°C, Corros. Sci. 57 (2012) 114.

[52] E.A. Gulbransen, K.F. Andrew, Kinetics of the Oxidation of Pure Tungsten from 500° to 1300°C, J. Electrochem. Soc. 107 (1960) 619.

[53] A. Chambers, Modern Vacuum Physics, CRC Press, 2004.

[54] I. Horcas, R. Fernández, J.M. Gómez-Rodríguez, J. Colchero, J. Gómez-Herrero, A. M. Baro, WSXM: A software for scanning probe microscopy and a tool for nanotechnology, Rev. Sci. Instrum. 78 (2007), 013705.

[55] S. Kasap, C. Koughia, H. E. Ruda, in *Springer Handbook of Electronic and Photonic Materials*, DOI: 10.1007/978-3-319-48933-9_2 (Eds: S. Kasap, P. Capper), Springer International Publishing, Cham **2017**, p. 1.

[56] D. Gall, Electron mean free path in elemental metals, J. Appl. Phys. 119 (2016), 085101.

[57] G. Abadias, E. Chason, J. Keckes, M. Sebastiani, G.B. Thompson, E. Barthel, G. L. Doll, C.E. Murray, C.H. Stoessel, L. Martinu, Review Article: Stress in thin films and coatings: current status, challenges, and prospects, J. Vac. Sci. Technol. A 36 (2018), 020801.

[58] L.B. Freund, S. Suresh, Thin Film Materials: Stress, Cambridge University Press, Cambridge, Defect Formation and Surface Evolution, 2004.

[59] J.S. Tello, A.F. Bower, E. Chason, B.W. Sheldon, Kinetic Model of Stress Evolution during Coalescence and Growth of Polycrystalline Thin Films, Phys. Rev. Lett. 98 (2007), 216104.

[60] C.V. Thompson, R. Carel, Stress and grain growth in thin films, J. Mech. Phys. Solids 44 (1996) 657.

[61] C.V. Thompson, Structure Evolution During Processing of Polycrystalline Films, Annu. Rev. Mater. Sci. 30 (2000) 159.

[62] V. Consonni, G. Rey, H. Roussel, D. Bellet, Thickness effects on the texture development of fluorine-doped SnO_2 thin films: the role of surface and strain energy, J. Appl. Phys. 111 (2012), 033523.

[63] D. Choi, X. Liu, P.K. Schelling, K.R. Coffey, K. Barmak, Failure of semiclassical models to describe resistivity of nanometric, polycrystalline tungsten films, J. Appl. Phys. 115 (2014), 104308.

[64] H.Z. Yu, C.V. Thompson, Grain growth and complex stress evolution during Volmer-Weber growth of polycrystalline thin films, Acta Mater. 67 (2014) 189.

[65] C.A. Davis, A simple model for the formation of compressive stress in thin films by ion bombardment, Thin Solid Films 226 (1993) 30.

[66] H. Windischmann, Intrinsic stress in sputter-deposited thin films, Crit. Rev. Solid State Mater. Sci. 17 (1992) 547.

[67] J.A. Thornton, D.W. Hoffman, Stress-related effects in thin films, Thin Solid Films 171 (1) (1989) 5–31.

[68] W.E. Lawrence, Electron-electron scattering in the low-temperature resistivity of the noble metals, Phys. Rev. B 13 (1976) 5316.

[69] R.T. Beach, R.W. Christy, Electron-electron scattering in the intraband optical conductivity of Cu, Ag, and Au, Phys. Rev. B 16 (1977) 5277.

[70] G.R. Parkins, W.E. Lawrence, R.W. Christy, Intraband optical conductivity of Cu, Ag, and Au: contribution from electron-electron scattering, Phys. Rev. B 23 (1981) 6408.

[71] T. Holstein, Theory of transport phenomena in an electron-phonon gas, Ann. Phys. 29 (1964) 410.

[72] T. Holstein, Optical and Infrared Volume Absorptivity of Metals, Phys. Rev. 96 (1954) 535.

[73] J.A. McKay, J.A. Rayne, Temperature dependence of the infrared absorptivity of the noble metals, Phys. Rev. B 13 (1976) 673.

[74] C.-Y. Young, The frequency and temperature dependence of the optical effective mass of conduction electrons in simple metals, J. Phys. Chem. Solids 30 (1969) 2765.

[75] B. Chakraborty, W.E. Pickett, P.B. Allen, Density of states, optical mass, and dc electrical resistance of Ta, W, Nb, and Mo using Slater-Koster interpolation, Phys. Rev. B 14 (1976) 3227.

[76] P. Romaniello, P.L. de Boeij, F. Carbone, D. van der Marel, Optical properties of bcc transition metals in the range, Phys. Rev. B 73 (2006), 075115.

[77] D.M. Arboleda, J.M.J. Santillán, L.J. Mendoza Herrera, D. Muraca, D.C. Schinca, L. B. Scaffardi, Size-dependent complex dielectric function of Ni, Mo, W, Pb, Zn and Na nanoparticles. Application to sizing, J. Phys. D Appl. Phys. 49 (2016), 075302.

[78] A. Kaidatzis, V. Psycharis, K. Mergia, D. Niarchos, Annealing effects on the structural and electrical properties of sputtered tungsten thin films, Thin Solid Films 619 (2016) 61.

[79] M. Chirumamilla, G.V. Krishnamurthy, S.S. Rout, M. Ritter, M. Störmer, A. Y. Petrov, M. Eich, Thermal stability of tungsten based metamaterial emitter under medium vacuum and inert gas conditions, Sci. Rep. 10 (2020) 3605.

[80] A.W. Bett, O.V. Sulima, GaSb photovoltaic cells for applications in TPV generators, Semicond. Sci. Tech. 18 (5) (2003) S184–S190.